



Effective orientation control of photogenerated carrier separation via rational design of a $\text{Ti}_3\text{C}_2(\text{TiO}_2)@\text{CdS}/\text{MoS}_2$ photocatalytic system

Zizheng Ai, Yongliang Shao, Bin Chang, Baibiao Huang, Yongzhong Wu*, Xiaopeng Hao*

State Key Lab of Crystal Materials, Shandong University, Jinan, 250100, PR China



ARTICLE INFO

Keywords:
 H_2 evolution
 Composite photocatalyst
 II junction
 Z-scheme
 Multi-step separation

ABSTRACT

Spontaneous photocatalytic H_2 evolution from solar-driven water splitting is highly attractive for converting abundant solar energy to valuable fuel. Regulation of the direction of photocarriers separation and transport is an important factor influencing solar energy conversion efficiency. Here, structural design and energy band engineering are employed to design and construct a novel $\text{Ti}_3\text{C}_2(\text{TiO}_2)@\text{CdS}/\text{MoS}_2$ composite photocatalyst. The transfer direction of photogenerated electrons and holes is achieved via rational conjunction of Ti_3C_2 and MoS_2 . This well designed photocatalytic system possesses remarkable H_2 evolution rate ($8.47 \text{ mmol h}^{-1} \text{ g}^{-1}$) and excellent photocatalytic stability. Furthermore, a high H_2 yield rate of $344.74 \mu\text{mol h}^{-1} \text{ g}^{-1}$ can be reached in pure water without any electron sacrificial agents. Through combination with the scope of a type II junction between CdS and MoS_2 , the new Z-scheme between CdS and TiO_2 transformed from Ti_3C_2 sets up a multi-step separation of electron-hole pairs. This process prolongs the lifetime of photogenerated electrons and makes them reach the active sites to initiate an efficient photocatalytic redox reaction. This work demonstrates that the design philosophy of selectively controlling the transfer direction of electrons and holes has promising applications in solar energy utilisation.

1. Introduction

Green generation of hydrogen (H_2) evolved from water splitting by using solar energy is an ideal future energy source to solve the energy crisis and ameliorate environmental pollution [1–4]. Therefore, the development of an efficient photocatalytic system for hydrogen evolution via photo-driving water splitting is a research emphasis in this field [5,6]. In the design and preparation of efficient semiconductor photocatalysts [7–9], CdS has long been studied as a potential photocatalyst for solar-driven water splitting to hydrogen due to its proper bandgap ($E_g = 2.42 \text{ eV}$) and appropriate band position [10–15]. Meanwhile, several inherent deficiencies (such as severe photo-corrosion, rapid charge carrier recombination and poor cycle stability) of CdS limit its application to large-scale solar hydrogen evolution reaction (HER) [16,17]. Different techniques have been developed to solve these issues. Utilising suitable co-catalysts with earth-abundant materials is an effective way to boost the activity and stability of CdS [18–21]. To date, although great progress in the development of earth-abundant co-catalysts has been achieved, some major issues originating from the intrinsic characteristics remain to be resolved. Firstly, the separation of photogenerated electron-hole pairs is limited by poor interface interaction [22]. Secondly, the random flow pathway of photogenerated

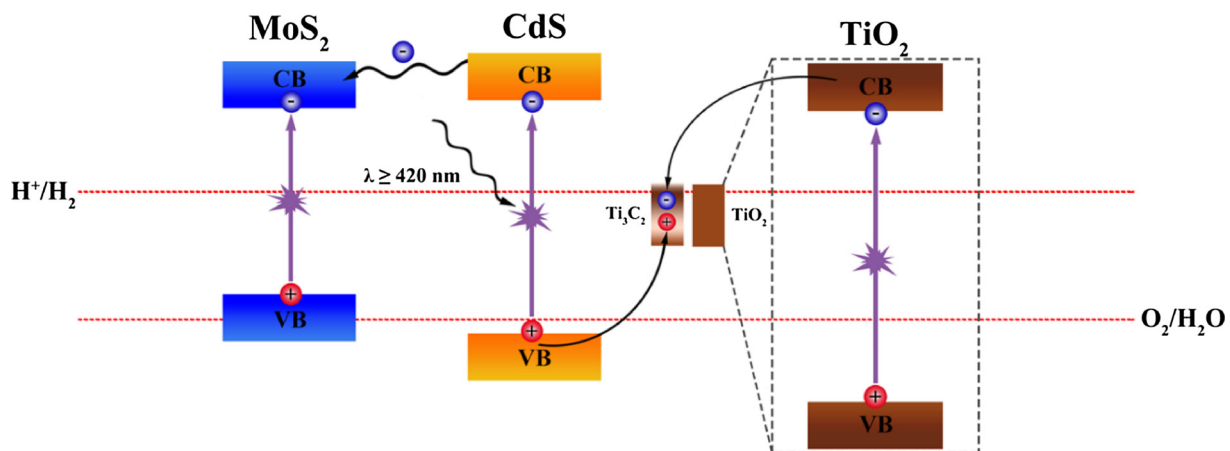
electrons and holes increases their recombination probability [23,24]. Thirdly, the spatial-directed separation for photogenerated electrons and holes needs to be improved and optimised. Therefore, suitable co-catalysts for constructing a photocatalytic system that can regulate photocarriers separation and transfer direction are needed. For this purpose, rational structural design and energy band matching are the important standards of references.

Molybdenum disulfide (MoS_2), a kind of two-dimensional (2D) transition metal dichalcogenide (TMD), possesses weak van der Waals bonding between two layers of hexagonally packed sulfur atoms. Physical or solvothermal exfoliation methods can gain MoS_2 nanosheets with single or few layers, which feature large specific surface areas for CdS nanoparticles growth and high electron mobility for efficient hydrogen evolution [25–28]. MoS_2 nanosheets also have a relatively low position of conduction band (CB) compared with CdS , which promotes the transfer of photo-electrons to MoS_2 nanosheets for H_2 evolution [29–31]. Therefore, MoS_2 nanosheets can be used as a co-catalyst to manipulate the transfer direction of photogenerated electrons.

Transition metal carbides (MXenes), a new type of 2D material via etching away the “A” groups from MAX phases, have exhibited promising capacity due to their great performance in energy storage and catalytic fields [32,33]. Ti_3C_2 , as a novel co-catalyst, has tremendous

* Corresponding authors.

E-mail addresses: wuyz@sdu.edu.cn (Y. Wu), xphao@sdu.edu.cn (X. Hao).



Scheme 1. Schematic illustrating the band structure of $\text{Ti}_3\text{C}_2(\text{TiO}_2)@\text{CdS}/\text{MoS}_2$ compound photocatalytic system.

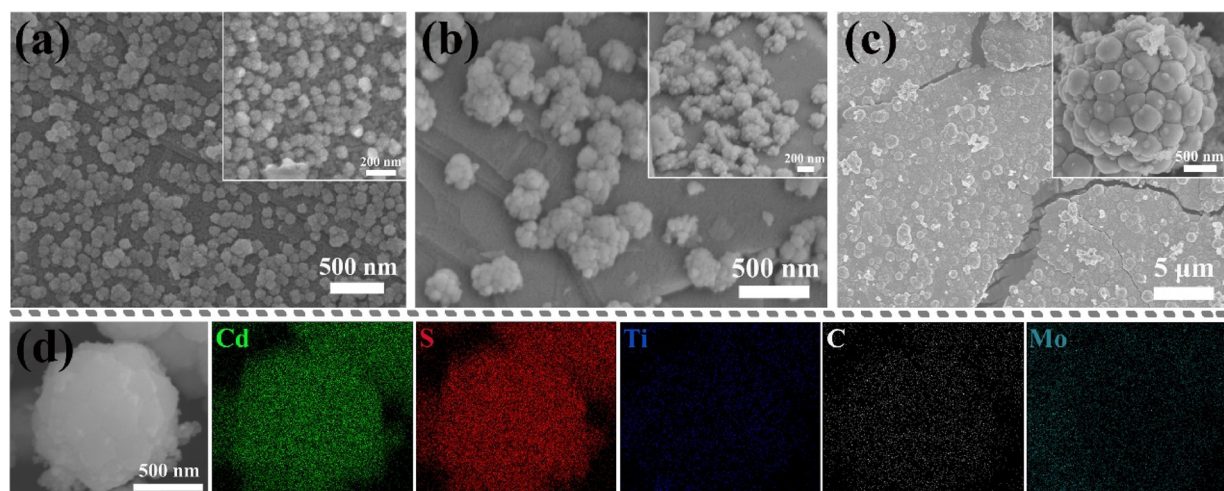


Fig. 1. SEM images of CMT-25-5 composites prepared with different hydrothermal times (a) 3 h, (b) 9 h, and (c) 12 h. (d) EDS elemental mapping images of Cd, S, Ti, C and Mo in CMT-25-5 composites.

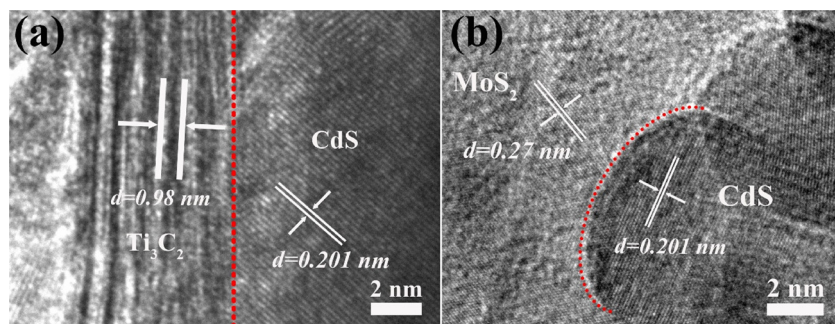


Fig. 2. HRTEM images of CMT-25-5 photocatalysts (prepared at 180 °C for 12 h). (a) $\text{CdS}@\text{Ti}_3\text{C}_2$. (b) CdS/MoS_2 .

potential to function well in HER due to its novel characteristics [34]. Abundant hydrophilic functionality enables Ti_3C_2 to form intimate contact with many semiconductors and possesses good interaction with solution. The termination groups with fluorine, hydroxyl or oxygen groups provide many active sites. And the excellent conductivity assures efficient charge-carrier transfer ability. In addition, the slight oxidation nature of Ti_3C_2 renders itself easy to capture photogenerated holes. The hydrogen evolution rate of $\text{TiO}_2/\text{Ti}_3\text{C}_2$ prepared by Wang delivered four times enhancement compared with pure rutile TiO_2 [35]. Yuan synthesised 2D-layered carbon/TiO₂ hybrids derived from Ti_3C_2 , which also showed good photocatalytic hydrogen evolution [36]. Thus,

as a next generation co-catalyst, Ti_3C_2 can serve as the mediator for controlling the transfer direction of photogenerated holes. In consideration of the above analysis, the advantages of Ti_3C_2 and MoS_2 are incorporated into CdS through rational structural design and energy band engineering to achieve a spatial-directed distribution of photogenerated electrons and holes.

Herein, we systematically designed and prepared a novel $\text{Ti}_3\text{C}_2(\text{TiO}_2)@\text{CdS}/\text{MoS}_2$ multi-material compound photocatalyst for the first time. Through a rational design of bifunctional co-catalyst (Ti_3C_2 , MoS_2) and morphology tuning of CdS, the precise amount and distribution of Ti_3C_2 and MoS_2 endow intimate interaction with CdS,

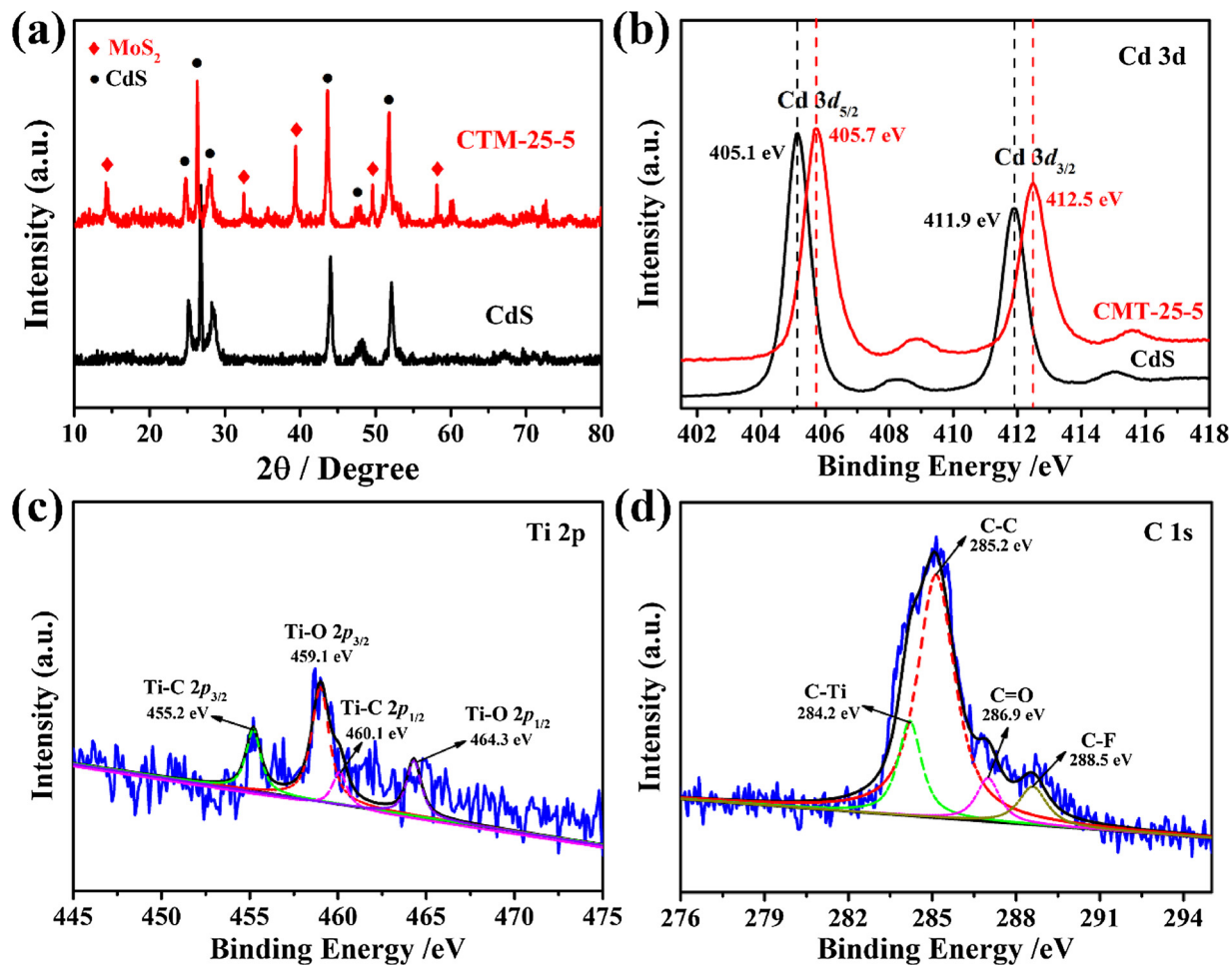


Fig. 3. (a) XRD patterns of pristine CdS and CMT-25-5 samples. High-resolution XPS spectra of (b) Cd 3d in pure CdS nanospheres and CMT-25-5. High-resolution XPS spectra of (c) Ti 2p and (d) C 1s in CMT-25-5.

which successfully achieves a superb high photocatalytic H₂ generation activity under visible light irradiation. The scope of a type II junction between CdS and MoS₂ and the Z-scheme between CdS and TiO₂ transformed from Ti₃C₂ set up a multi-step separation of electron-hole pairs, which further increases the H₂ evolution rate to 344.74 μmol h⁻¹ g⁻¹ in pure water without any sacrificial reagents. This innovative work provides a novel way to manipulate the electron and hole transfer direction efficiently via specific architecture design and band engineering.

2. Theory

The rational structural design plays a vital role in synthesising and controlling composite photocatalytic systems. Furthermore, the regulation of photocarriers separation and transfer direction is guided by band engineering theory. Integrating the above concepts, the schematic band structure is shown in Scheme 1. In the band configuration, the CB level of MoS₂ is lower than that of CdS. The photogenerated electrons can transfer from the CB of CdS to the CB of MoS₂, realising the first separation of electron-hole pairs. Meanwhile, Ti₃C₂ serves as the mediator for attracting holes because of its oxidation feature. Thus, the photogenerated holes of CdS move to Ti₃C₂, which reduces the probability of recombination. A new Z-scheme between CdS and TiO₂ transformed from Ti₃C₂ oxidation is gradually formed, thereby establishing the second separation of electron-hole pairs and prolonging the lifetime of photogenerated electrons greatly. Through rational structural design and morphology control, the compound photocatalytic system is further optimised. In a word, the spatial-directed separation of

photocarriers is achieved via this multi-step separation regulation.

3. Results and discussion

The typical synthesis route of Ti₃C₂(TiO₂)@CdS/MoS₂ (CMT-25-5) composites is as follows (Fig. S1). At first, Cd²⁺ and S²⁻ coalesce to form single CdS nanoparticles. Scanning electron microscopy (SEM) images show that the size of the initial CdS nanoparticles distributed on MoS₂ NSs is approximately 50 nm (Fig. 1a). As a platform, MoS₂ NSs can provide many amicable sites for the further growth of CdS. Compared with the bulk MoS₂, MoS₂ NSs (Fig. S2) possess large specific surface area and quick electron mobility. As the hydrothermal time is prolonged, single CdS nanoparticles merge together under the driving of thermodynamics (Fig. 1b). Meanwhile, Ti₃C₂ NSs (Fig. S3) gradually attach onto the surface of the initial CdS nanospheres. With an appropriate hydrothermal time, Ti₃C₂@CdS nanosphere clusters with suitable size form on MoS₂ NSs (Figs. 1c, S4). Ultimately, the composite photocatalyst of CMT-25-5 is successfully prepared. Energy dispersive X-ray spectrometry (EDS) mapping analysis shows the presence and homogeneous distribution of Cd, S, Ti, C and Mo in Ti₃C₂@CdS nanosphere clusters (Fig. 1d). Different doping ratios of Ti₃C₂ and MoS₂ NSs were utilised to study the specific formation mechanism of CdS nanospheres. It can be seen (Fig. S5) that the homogeneous CdS nanospheres are distributed on MoS₂ NSs with a suitable doping concentration. An appropriate coverage of Ti₃C₂ NSs can maintain adequate interaction with CdS and full utilisation of incident light (Fig. S6). Furthermore, the change in crystallinity of CMT-25-5 displays that the hydrothermal reaction at 180 °C is the optimal (Fig. S7).

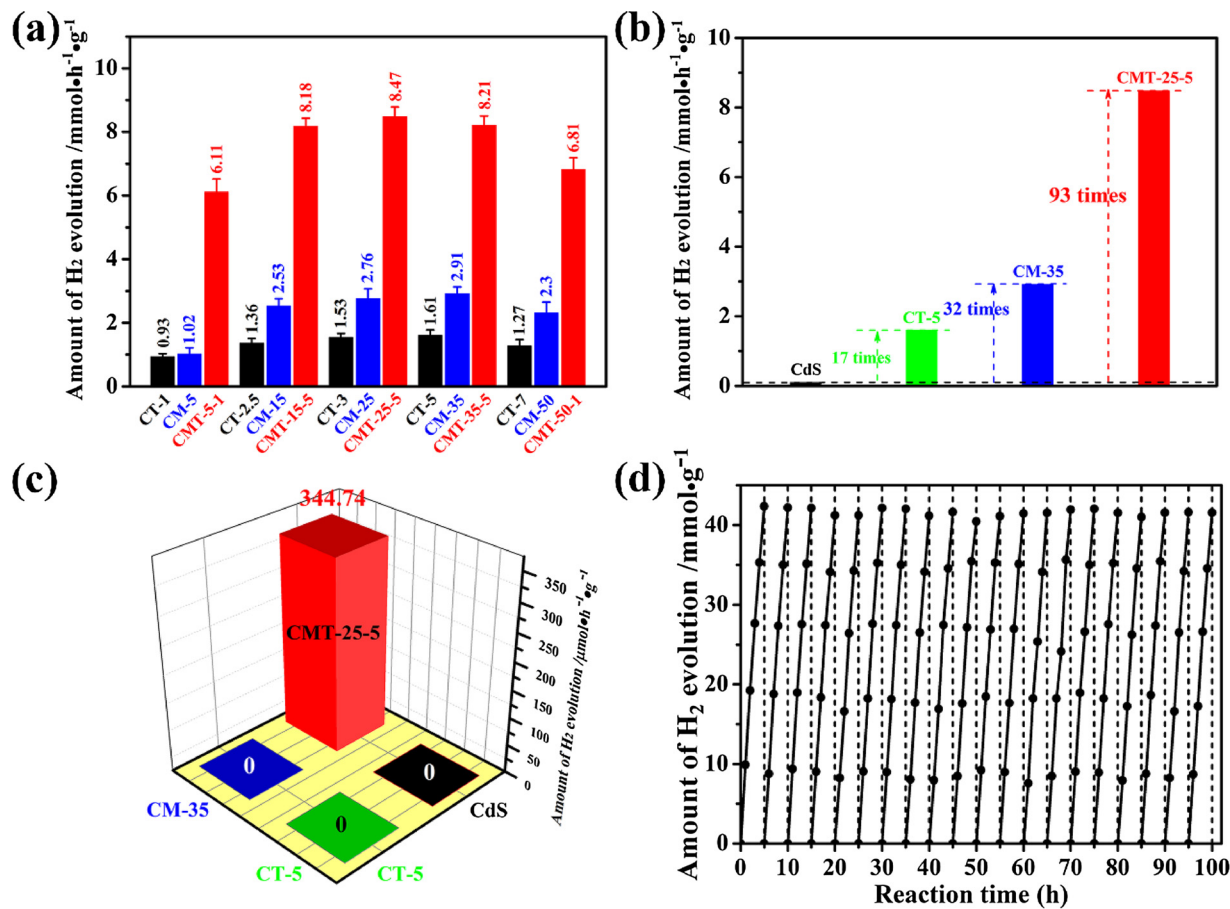


Fig. 4. (a) Comparison of activity of photocatalytic hydrogen evolution with different amounts of deposited Ti_3C_2 and MoS_2 NSs. (b) Photocatalytic H_2 evolution activities of pristine CdS, CT-5, CM-35 and CMT-25-5 samples. (c) H_2 evolution rate comparison of pristine CdS, CT-5, CM-35 and CMT-25-5 samples in pure water. (d) Recycling photocatalytic H_2 evolution test of CMT-25-5.

The structure of the composite was further analysed via High resolution transmission electron microscope (HRTEM) to observe the lattice fringes corresponding to different samples. The characteristic lattice spacings of 0.98 and 0.27 nm are assigned to the (002) plane of Ti_3C_2 NSs [37] and the (100) facet of MoS_2 NSs, respectively (Fig. S8). The number of layers of Ti_3C_2 NSs keeps a certain level (four or five layers) after ultrasonic treatment (Fig. S9a). This condition provides large contact area and good interaction with CdS nanospheres. The (110) facet of hexagonal CdS nanospheres possesses the lattice spacing of 0.201 nm [38,39]. The HRTEM image in Fig. 2a shows an evident interface with lattice spacings of 0.98 and 0.201 nm, which correspond to the (002) plane of Ti_3C_2 NSs and the (110) plane of CdS. In addition, Fig. 2b proves the existence of the interface between CdS and MoS_2 with the (100) plane of MoS_2 and the (110) plane of CdS. The results confirm that Ti_3C_2 and MoS_2 NSs are combined well with CdS. Remarkably, a Ti_3C_2 fragment is deposited on the surface of CdS nanospheres (Fig. S9). Furthermore, the flexibility feature of Ti_3C_2 NSs (Fig. S10) enables strong adhesion to the CdS surface.

X-ray diffraction (XRD) was conducted to determine the crystal structures of the as-prepared samples. Fig. 3a shows that CdS nanospheres with hexagonal wurtzite-structured phase exhibit three characteristic diffraction peaks (100), (002) and (101) at 25.1° , 26.7° and 28.4° , respectively. Notably, the CMT-25-5 composite possesses typical diffraction peaks of MoS_2 NSs. However, no peaks of Ti_3C_2 NSs can be detected, which can be ascribed to the relatively low loading and dispersion nature of Ti_3C_2 NSs (Figs. S11 and S12). The crystal structure of CdS can still remain unchanged after being combined with Ti_3C_2 and MoS_2 NSs. This phenomenon indicates that the improved photocatalytic activity is due to Ti_3C_2 and MoS_2 NSs deposited on the CdS surface

instead of crystal structure alteration.

Furthermore, Raman spectroscopy and X-ray photoelectron spectroscopy (XPS) were carried out to analyse the CMT-25-5 structure. The Raman spectra of Ti_3C_2 , MoS_2 and CMT-25-5 imply their successful incorporation with CdS (Fig. S13). Moreover, XPS was used to investigate the composition and electronic structure of CMT-25-5. The full XPS spectrum consists of Cd, S, Mo, Ti and C (Fig. S14). The high-resolution XPS spectrum of Cd 3d (Fig. 3b) shows two peaks at 412.5 and 405.7 eV, which correspond to the characteristic binding energies of Cd^{2+} $3d_{3/2}$ and Cd^{2+} $3d_{5/2}$, respectively. Compared with the Cd signal at 411.9 and 405.1 eV in pure CdS, the shift towards high energy indicates the possible interaction between Ti_3C_2 and MoS_2 NSs with CdS nanospheres. In the S 2p XPS spectrum (Fig. S15a), the peaks at 161.9 and 163.1 eV correspond to S^{2-} . The high-resolution XPS spectrum of Mo 3d (Fig. S15b) displays two peaks at 229.2 and 232.3 eV, which can be assigned to Mo^{4+} $3d_{5/2}$ and Mo^{4+} $3d_{3/2}$. The peak at 226.4 eV matches well with the binding energy of S 2s in sulfides. Moreover, the high-resolution XPS spectrum of Ti 2p exhibits four deconvoluted peaks (Fig. 3c), corresponding to Ti-O 2p and Ti-C 2p. The high-resolution XPS spectrum of C 1s (Fig. 3d) also suggests the functionalization of $-\text{O}-\text{OH}$ on Ti_3C_2 NSs after hydrothermal treatment. Together with SEM and TEM observations, these results all corroborate that CMT-25-5 is prepared successfully via a rational structural design.

The photocatalytic H_2 production activity of the samples was examined under visible light ($\lambda \geq 420$ nm). As shown in Fig. 4a, the samples with various ratios of MoS_2 and Ti_3C_2 show different performances of H_2 production, wherein CMT-25-5 exhibits the optimal performance. In Fig. 4b, pure CdS exhibits a poor photocatalytic activity of $0.0916 \text{ mmol h}^{-1} \text{ g}^{-1}$ due to its inherent photo-corrosion.

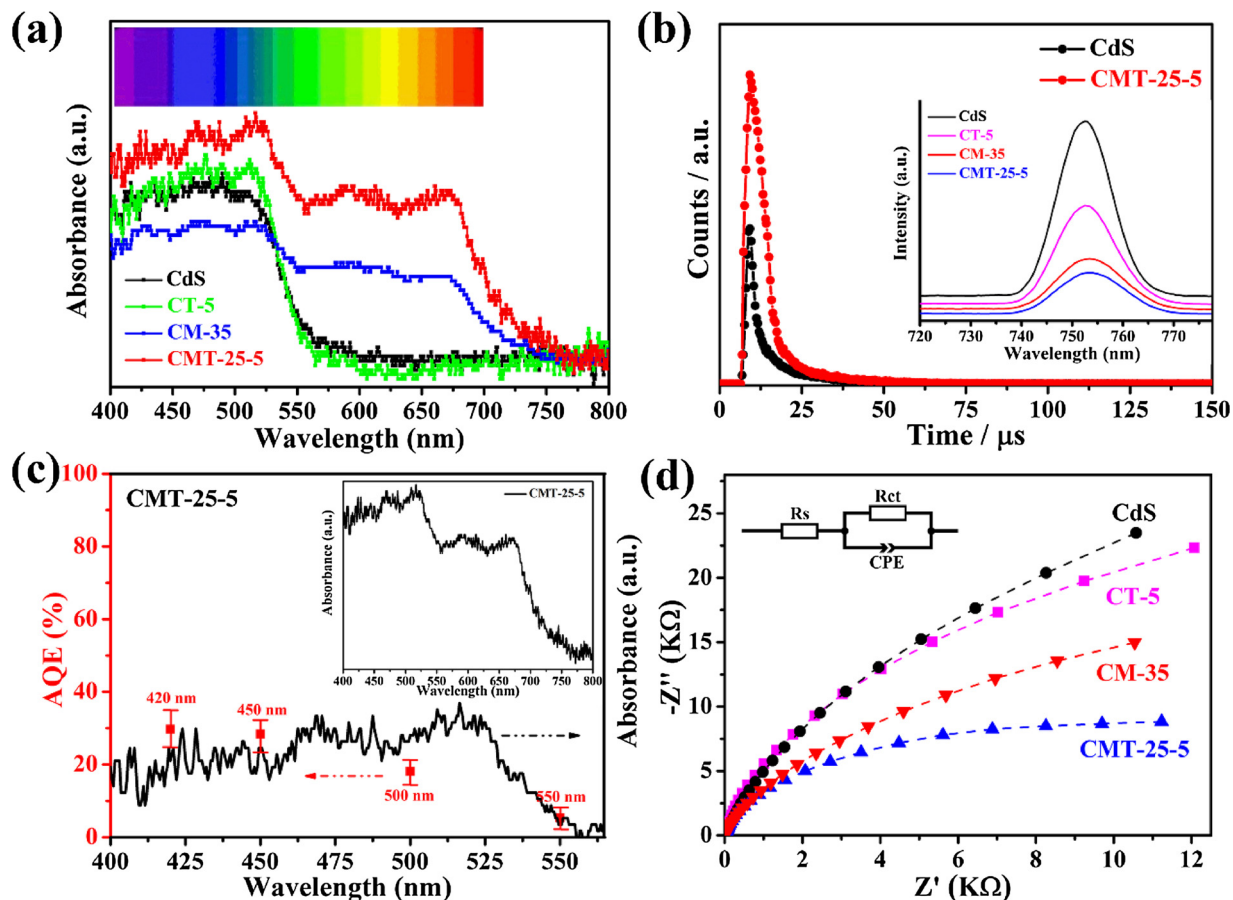


Fig. 5. (a) UV-vis diffuse reflectance spectra of pristine CdS, CT-5, CM-35 and CMT-25-5. (b) Fluorescent lifetime spectra of pristine CdS and CMT-25-5, inset: Room temperature (298 K) steady-state PL spectra of pristine CdS, CT-5, CM-35 and CMT-25-5. (c) UV-vis diffuse reflectance spectrum (black) and quantum efficiency (red dots) of CMT-25-5. (d) Nyquist impedance plots of pristine CdS, CT-5, CM-35 and CMT-25-5, inset: An electrical equivalent circuit diagram. (For interpretation of the references to colour in this figure legend, the reader is referred to the web version of this article.)

Loading a certain amount of Ti_3C_2 NSs (CT-5) or MoS_2 NSs (CM-35) can improve the photocatalytic activity to 1.604 and 2.914 $\text{mmol h}^{-1} \text{g}^{-1}$, which are 17 and 32 times higher than those of the initial sample (CdS), respectively. However, an appropriate structural design of $\text{Ti}_3\text{C}_2(\text{TiO}_2)$ @CdS/ MoS_2 can exert a synergistic effect, which greatly boosts the photocatalytic activity of CdS. As a consequence, CMT-25-5 achieves a dramatically high photocatalytic H_2 activity of 8.47 $\text{mmol h}^{-1} \text{g}^{-1}$, which exceeds that of CdS by 93 times. This surprising result shows the superior effect on their sole operation. The photocatalytic H_2 production activity with different loading amounts of MoS_2 or Ti_3C_2 NSs was investigated (Fig. S16). Among the samples, CMT-25-5 shows the best HER activity and can be further optimised by regulating the hydrothermal temperature and time (Figs. S17 and S18). This result indicates that the charge separation and transfer direction can be effectively manipulated by rational specific construction design.

Even more amazing, Fig. 4c shows that the H_2 production activity of CMT-25-5 can still reach 344.74 $\mu\text{mol h}^{-1} \text{g}^{-1}$ in pure water splitting without any sacrificial agents. By contrast, CT-5 and CM-35 do not show any H_2 production activity. This distinction proves that the $\text{Ti}_3\text{C}_2(\text{TiO}_2)$ @CdS/ MoS_2 compound system can effectively regulate the direction of separated electron-hole pairs and prolong the lifetime of electrons, whereas single construction of CdS@ Ti_3C_2 or CdS/ MoS_2 cannot reach the above goals. Furthermore, CMT-25-5 exhibits the highest photocatalytic activity with different ratios of Ti_3C_2 and MoS_2 NSs (Fig. S19). This designed system still exhibits the unique superiority especially in pure water in comparison to the previously reported CdS-based composite photocatalysts (Table S1).

The recyclability of the optimised CMT-25-5 was estimated by

repeating intermittent H_2 evolution under simulated solar light. On the one hand, H_2 production activity can maintain high stability after 100 h, and 98% of incipient production can be preserved in a 20% lactic acid solution (Fig. 4d). Moreover, the long stability test shows that the high H_2 evolution level maintains high stability even after 300 h (Fig. S20). On the other hand, 90% of photocatalytic activity can still be preserved after 40 h in pure water (Fig. S21). The excellent stability is attributed to the unique robust construction. This aspect will be discussed in detail in the following section.

Understanding the mechanism of photocatalytic reaction is important to further study the origin of the remarkable activity of CMT-25-5. Firstly, light absorption plays a vital role as a precondition for H_2 production. The solar light harvesting of CMT-25-5 was investigated via UV-vis absorption spectrum. As shown in Fig. 5a, the CdS nanospheres exhibit poor absorbance intensity. The absorption of CT-5 also has a similar curve, which can be confirmed again in other proportions (Fig. S22a). The semiconducting property of MoS_2 NSs contributes to the absorption enhancement. In Fig. S23, the UV-vis absorption spectrum of MoS_2 shows stronger intensity than Ti_3C_2 . Thus, the light absorption of CM-35 reveals an enhancive region of 550–750 nm. Furthermore, this trend can be observed in different doping ratios (Fig. S22b). Compared with their absorption spectra, CMT-25-5 presents a higher and broader absorption region from 550 nm to 700 nm stemming from the specific structure and energy band matching. Therefore, the incident sunlight will be utilised at the maximum for the following photon excitation. Secondly, the separation of electron-hole pairs and transfer are the next key processes. Thus, the charge separation and transfer efficiency of CMT-25-5 were studied by a series of

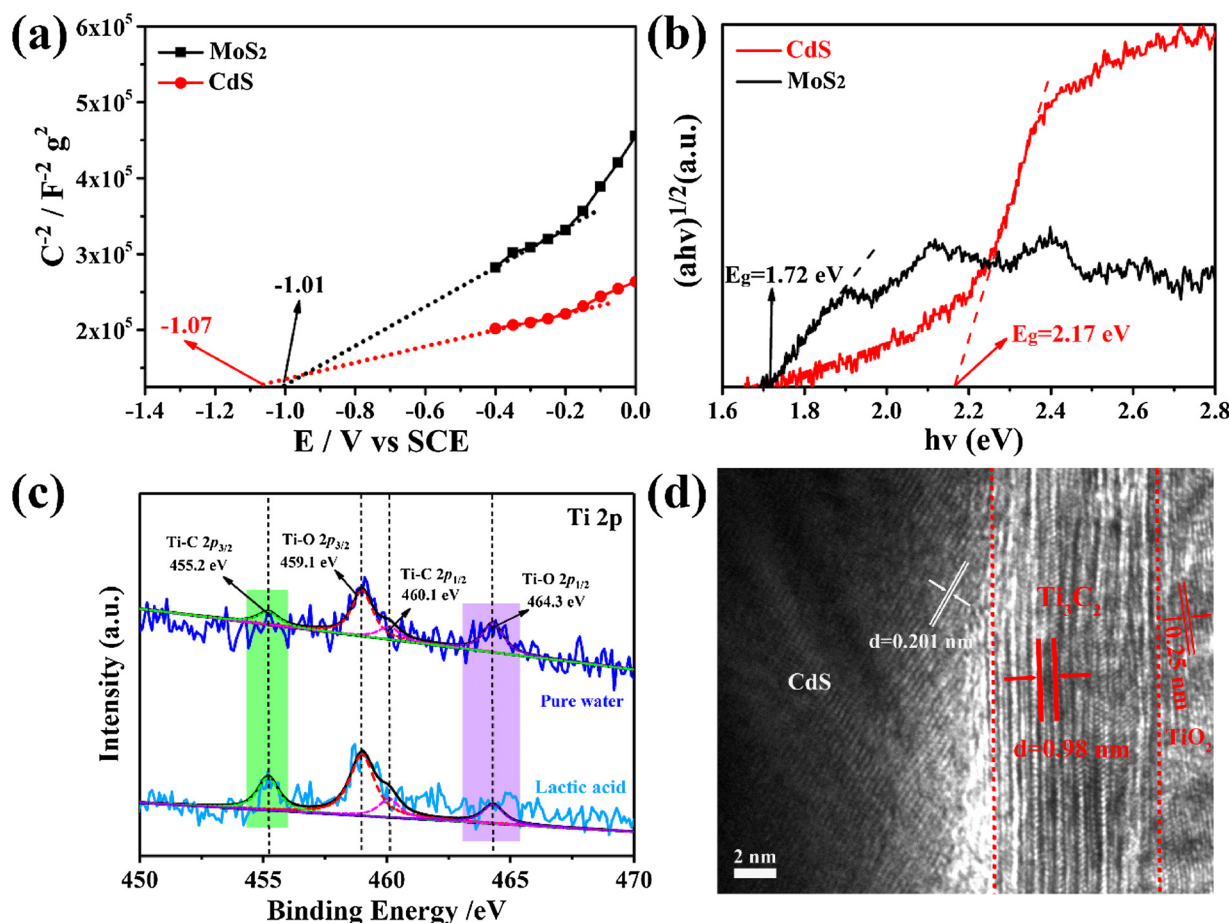


Fig. 6. (a) Mott-Schottky plots of MoS₂ NSs and CdS. (b) $(ahv)^{1/2}$ plots versus $h\nu$ for MoS₂ NSs and CdS. (c) Ti 2p XPS spectra contrast of CMT-25-5 in pure water and lactic acid. (d) HRTEM image of CMT-25-5 during HER in pure water.

characterisation techniques. As shown in Fig. 5b, the time-resolved photoluminescence (TRPL) spectrum of CMT-25-5 displays a longer lifetime than that of CdS. In addition, the comparison of lifetimes among CdS, CT-5, CM-35 and CMT-25-5 is displayed in Fig. S24, which indicates that the lifetime can be further prolonged by integrating with Ti₃C₂ and MoS₂. Furthermore, the steady-state photoluminescence (PL) spectra of the obtained materials were recorded to study the recombination of photogenerated charge pairs (Fig. 5b, inset). The emission peak of CMT-25-5 shows no shift in comparison with CdS. At the same time, its quenched emission peak at 754 nm, which is weaker than other samples, can be assigned to deep level interstitial-site and antisite defects [40]. This finding also confirms its enhanced charge separation efficiency. Fig. 5c shows the apparent quantum efficiency (AQE) values for H₂ evolution of the CMT-25-5 photocatalyst under different monochromatic light irradiations. The AQE values of H₂ production were calculated to be 29.7%, 28.4%, 18.1% and 5.3% at 420, 450, 500 and 550 nm, respectively. This result matches well with the diffuse reflectance spectrum of CMT-25-5 (Fig. 5c, inset). The high AQE obtained by CMT-25-5 probably originates from the unique structure with a suitable energy band matching. As a result, photogenerated excitons are promoted to take part in the redox reaction, suppressing non-productive charge recombination. Therefore, this compound photocatalyst has potential in harnessing sunlight. Moreover, the interfacial charge-carrier separation and transfer efficiencies were investigated by electrochemical impedance spectroscopy (EIS). The diagrams of the arc radius on the EIS Nyquist plots of the samples are shown in Fig. 5d, and the semicircles in the Nyquist plots can be simulated well by an electrical equivalent circuit diagram (Fig. 5d, inset) [41,42]. CMT-25-5 shows a smaller semicircle radius and lower interfacial charge transfer

resistance than CdS, CT-5 and CM-35, indicating the distinct improvement of interfacial charge-carrier separation and transfer. The transient photocurrent (TPC) response was also conducted to probe the separation efficiency of electron-hole pairs (Fig. S25). In several on-off cycles of irradiation, CMT-25-5 exhibits high photocurrent response, suggesting that the recombination of the photogenerated charge carriers is suppressed effectively.

In-depth understanding of the charge separation and transfer mechanism of CMT-25-5 is significant. The proper bandgap structure plays a crucial role. CMT-25-5 takes on a smaller bandgap than CT-5 and CM-35, indicating that great amount of sunlight can be absorbed to take part in the activated process (Fig. S26). The position of CB and valence band (VB) plays a decisive role in the separation of electron-hole pairs and transfer direction. For this purpose, the Mott-Schottky of CdS and MoS₂ NSs was conducted to study their electronic band structure (Fig. 6a). Notably, they all exhibit the feature of n-type semiconductors. According to the x-intercept in the MS plot, the potential of the CB edge (E_{CB}) is approximately estimated. The E_{CB} values of CdS and MoS₂ NSs were calculated to be -1.07 V vs. SCE (-0.83 V vs. NHE) and -1.01 V vs. SCE (-0.76 V vs. NHE), respectively. Combined with the plot of the Kubelka-Munk function $[ahv]^{1/2}$ versus the energy of absorbed light converted from the UV-vis absorption spectrum [43], the bandgaps of CdS and MoS₂ NSs were determined to be 2.17 and 1.72 eV (Fig. 6b), respectively. Incorporating the above analysis, the E_{VB} of CdS and MoS₂ NSs can be speculated to be 1.34 and 0.96 eV, respectively. The results confirm that the CB of CdS is above that of MoS₂ NSs. The band alignment of CdS and MoS₂ NSs forms the scope of a type II junction (Fig. S27) [44]. On the basis of the above analysis, the energy level diagram of CMT-25-5 is presented in Fig. S28. The different levels of

band structures drive the separated electrons to MoS₂ NSs with the low CB edge. The charge recombination can be suppressed due to the consistent charge migrations inside and outside the space charge region. In addition, Ti₃C₂ NSs serve as the mediator for attracting holes because of their oxidation feature [45]. They can work as a hole trapping and shuttling sites. On the one hand, Ti₃C₂ NSs spread over the surface of CdS nanospheres, increasing the number of paths to Ti₃C₂ NSs. On the other hand, the separated holes in CdS migrate to Ti₃C₂ NSs via these paths. This condition suppresses the charge recombination and prolongs the lifetime of photogenerated electrons. Finally, the separated photogenerated electrons transfer to MoS₂ NSs for HER, and photogenerated holes move to Ti₃C₂ NSs for the oxidization of sacrificial agents. Thus, the excellent HER activity is achieved by the synergistic effect of the CMT-25-5 system. The corresponding photocatalytic mechanism illustration of CMT-25-5 for hydrogen production under visible light irradiation is shown in Fig. S29. In addition, the XRD pattern contrast of CMT-25-5 (Fig. S30) confirms that this specific structure remains robust in the entire HER process. At the same time, Ti₃C₂ NSs can retain their integrity (Fig. S31). Compared with the above mechanism analysis, the photocatalytic mechanism of CMT-25-5 in pure water is different as depicted in Fig. S32. Throughout this process, O₂ was not detected in this system. This result indicates that the oxidation potential for –OH to O₂ is unfavored in thermodynamics. The photogenerated holes participate in –OH oxidation. Then, –OH is oxidized to ·OH radicals. Electron spin resonance (ESR) measurement was conducted to prove the speculation. As shown in Fig. S33, the DMPO-OH signal of CMT-25-5 in pure water can be detected after 30 min of visible light irradiation. In addition, Fig. 6c shows that the peak of Ti–O 2p_{1/2} in pure water increases evidently compared with the peak of Ti–O 2p_{1/2} in lactic acid, indicating the formation of TiO₂ during HER in pure water. At the same time, Fig. 6d clearly shows that a layer of TiO₂ gradually is formed on the surface of the Ti₃C₂ NSs surface during oxidation. As a consequence, the Z-scheme between TiO₂ and CdS is gradually formed and participates in HER, building a multi-step separation of electron-hole pairs and further enhancing the hydrogen production. Besides, as the shield, it can postpone the oxidation of Ti₃C₂ NSs. The HRTEM (Fig. S34) demonstrates that Ti₃C₂ NSs are still preserved with a layer of TiO₂ after 40 h of reaction. Given the above situations, this unique designed composite photocatalyst shows a potential in photochemical water splitting.

4. Conclusion

In this work, we designed and fabricated a novel Ti₃C₂(TiO₂)@CdS/MoS₂ composite photocatalyst via a facile hydrothermal method. The regulation of charge separation and transfer direction was achieved successfully under the guidance of the structural design and energy band engineering. The hybrid photocatalyst demonstrates remarkable photocatalytic H₂ production activity (8.47 mmol h⁻¹ g⁻¹) and excellent photocatalytic stability. The Z-scheme between CdS and TiO₂ transformed from Ti₃C₂ is gradually formed in pure water, further making it useful to photocatalytic pure water splitting without any electron sacrificial agents. Multi-step separation of electron-hole pairs is the key point for initiating photocatalytic water splitting. This study opens a new pathway to construct an effective composite photocatalytic system for water splitting reactions.

Acknowledgements

This work is supported by the National Natural Science Foundation of China (Contract Nos. 51572153, 51602177), the Major Basic Program of the Natural Science Foundation of Shandong Province (Contract No. ZR2017ZB0317) and Taishan Scholars Program of Shandong Province.

Appendix A. Supplementary data

Supplementary material related to this article can be found, in the online version, at doi:<https://doi.org/10.1016/j.apcatb.2018.09.101>.

References

- [1] K. Maeda, K. Teramura, D. Lu, T. Takata, N. Saito, Y. Inoue, K. Domen, *Nature* (2006) 295.
- [2] X. Chen, S. Shen, L. Guo, S.S. Mao, *Chem. Res.* 110 (2010) 6503–6570.
- [3] J. Chen, X.J. Wu, L. Yin, B. Li, X. Hong, Z. Fan, B. Chen, C. Xue, H. Zhang, *Angew. Chem. Int. Ed.* 54 (2015) 1210–1214.
- [4] R.M. Navarro, M.C. Sánchez-Sánchez, M.C. Alvarez-Galvan, F. del Valle, J.L.G. Fierro, *Energy Environ. Sci.* 2 (2009) 35–54.
- [5] J.R. McKone, S.C. Marinescu, B.S. Brunschwig, J.R. Winkler, H.B. Gray, *Chem. Sci.* 5 (2014) 865–878.
- [6] M.S. Faber, S. Jin, *Energy Environ. Sci.* 7 (2014) 3519–3542.
- [7] H. Ou, P. Yang, L. Lin, M. Anpo, X. Wang, *Angew. Chem. Int. Ed.* 56 (2017) 10905–10910.
- [8] G. Zhang, G. Li, Z.-A. Lan, L. Lin, A. Savateev, T. Heil, S. Zafeiratos, X. Wang, M. Antonietti, *Angew. Chem. Int. Ed.* 56 (2017) 13445–13449.
- [9] S.R. Lingampalli, U.K. Gautam, C.N.R. Rao, *Energy Environ. Sci.* 6 (2013) 3589–3594.
- [10] F. Huang, J. Hou, H. Wang, H. Tang, Z. Liu, L. Zhang, Q. Zhang, S. Peng, J. Liu, G. Cao, *Nano Energy* 32 (2017) 433–440.
- [11] G. Wang, X. Yang, F. Qian, J.Z. Zhang, Y. Li, *Nano Lett.* 10 (2010) 1088–1092.
- [12] X. Zong, H. Yan, G. Wu, G. Ma, F. Wen, L. Wang, C. Li, *J. Am. Chem. Soc.* 130 (2008) 7176–7177.
- [13] L. Jia, D.-H. Wang, Y.-X. Huang, A.-W. Xu, H.-Q. Yu, *J. Phys. Chem. C* 115 (2011) 11466–11473.
- [14] R. Shi, H.-F. Ye, F. Liang, Z. Wang, K. Li, Y. Weng, Z. Lin, W.-F. Fu, C.-M. Che, Y. Chen, *Adv. Mater.* 30 (2018) 1705941.
- [15] B. Ma, H. Xu, K. Lin, J. Li, H. Zhang, W. Liu, C. Li, *ChemSusChem* 9 (2016) 820–824.
- [16] P. Kalisman, Y. Nakibli, L. Amirav, *Nano Lett.* 16 (2016) 1776–1781.
- [17] J. Yang, H. Yan, X. Wang, F. Wen, Z. Wang, D. Fan, J. Shi, C. Li, *J. Catal.* 290 (2012) 151–157.
- [18] J. Ran, J. Zhang, J. Yu, M. Jaroniec, S.Z. Qiao, *Chem. Soc. Rev.* 43 (2014) 7787–7812.
- [19] Y. Hou, B.L. Abrams, P.C.K. Vesborg, M.E. Björketun, K. Herbst, L. Bech, A.M. Setti, C.D. Damsgaard, T. Pedersen, O. Hansen, J. Rossmeisl, S. Dahl, J.K. Nørskov, I. Chorkendorff, *Nat. Mater.* 10 (2011) 434–438.
- [20] D. Ma, J.-W. Shi, Y. Zou, Z. Fan, X. Ji, C. Niu, L. Wang, *Nano Energy* 39 (2017) 183–191.
- [21] G. Han, Y.-H. Jin, R.A. Burgess, N.E. Dickenson, X.-M. Cao, Y. Sun, *J. Am. Chem. Soc.* 139 (2017) 15584–15587.
- [22] N.R. Monahan, K.W. Williams, B. Kumar, C. Nuckolls, X.-Y. Zhu, *Phys. Rev. Lett.* 114 (2015) 247003.
- [23] J.M. Elward, A. Chakraborty, *J. Chem. Theory Comput.* 11 (2015) 462–471.
- [24] J.K. Utterback, M.B. Wilker, K.A. Brown, P.W. King, J.D. Eaves, G. Dukovic, *Phys. Chem. Chem. Phys.* 17 (2015) 5538–5542.
- [25] X. Liu, Z. Xing, H. Zhang, W. Wang, Y. Zhang, Z. Li, X. Wu, X. Yu, W. Zhou, *ChemSusChem* 9 (2016) 1118–1124.
- [26] M. Jahurul Islam, D. Amaranatha Reddy, N.S. Han, J. Choi, J.K. Song, T.K. Kim, *Phys. Chem. Chem. Phys.* 18 (2016) 24984–24993.
- [27] Y. Liu, Y.-X. Yu, W.-D. Zhang, *J. Phys. Chem. C* 117 (2013) 12949–12957.
- [28] S. Ma, J. Xie, J. Wen, K. He, X. Li, W. Liu, X. Zhang, *Appl. Surf. Sci.* 391 (2017) 580–591.
- [29] F. Ma, Y. Wu, Y. Shao, Y. Zhong, J. Lv, X. Hao, *Nano Energy* 27 (2016) 466–474.
- [30] J. Zhang, Z. Zhu, X. Feng, *Chem. Eur. J.* 20 (2014) 10632–10635.
- [31] A. Wu, C. Tian, Y. Jiao, Q. Yan, G. Yang, H. Fu, *Appl. Catal. B: Environ.* 203 (2017) 955–963.
- [32] M. Ghidui, M.R. Lukatskaya, M.-Q. Zhao, Y. Gogotsi, M.W. Barsoum, *Nature* 516 (2014) 78–81.
- [33] M.R. Lukatskaya, O. Mashtalir, C.E. Ren, Y. Dall'Agnese, P. Rozier, P.L. Taberna, M. Naguib, P. Simon, M.W. Barsoum, Y. Gogotsi, *Science* 341 (2013) 1502–1505.
- [34] J. Ran, G. Gao, F.-T. Li, T.-Y. Ma, A. Du, S.-Z. Qiao, *Nat. Commun.* 8 (2017) 13907.
- [35] H. Wang, R. Peng, Z.D. Hood, M. Naguib, S.P. Adhikari, Z. Wu, *ChemSusChem* 9 (2016) 1490–1497.
- [36] W. Yuan, L. Cheng, Y. Zhang, H. Wu, S. Lv, L. Chai, X. Guo, L. Zheng, *Adv. Mater. Interface* 4 (2017) 1700577.
- [37] T.Y. Ma, J.L. Cao, M. Jaroniec, S.Z. Qiao, *Angew. Chem. Int. Ed.* 55 (2016) 1138–1142.
- [38] H. Chauhan, Y. Kumar, J. Dana, B. Satpati, H.N. Ghosh, S. Deka, *Nanoscale* 8 (2016) 15802–15812.
- [39] Y. Li, X. Li, C. Yang, Y. Li, *J. Mater. Chem.* 13 (2003) 2641–2648.
- [40] S. Na-Phattalung, M.F. Smith, K. Kim, M.-H. Du, S.-H. Wei, S.B. Zhang, S. Limpijumnong, *Phys. Rev. B* 73 (2006) 125205.
- [41] L. Sun, L. Xiang, X. Zhao, C.-J. Jia, J. Yang, Z. Jin, X. Cheng, W. Fan, *ACS Catal.* 5 (2015) 3540–3551.
- [42] H. He, R. Xiong, J. Fan, *Energies* 4 (2011) 582–598.
- [43] W. Zhao, W. Ma, C. Chen, J. Zhao, Z. Shuai, *J. Am. Chem. Soc.* 126 (2004) 4782–4783.
- [44] D. Sarkar, C.K. Ghosh, S. Mukherjee, K.K. Chattopadhyay, *ACS Appl. Mater. Inter.* 5 (2013) 331–337.
- [45] A.N. Enyashin, A.L. Ivanovskii, *Comput. Theor. Chem.* 989 (2012) 27–32.